Robust formation of skyrmion and skyrmionium in magnetic hemispherical shells and their dynamic switching

Jaehak Yang,[1] Hyeon-Kyu Park,[1] Gyuyoung Park,[1] Claas Abert,[2,3] Dieter Suess,[2,3] and Sang-Koog Kim[1,*]

[1]*National Creative Research Initiative Center for Spin Dynamics and Spin-Wave Devices, Nanospinics Laboratory, Research Institute of Advanced Materials, Department of Materials Science and Engineering, Seoul National University, Seoul 151-744, South Korea*

[2]*Faculty of Physics, University of Vienna, Vienna, Austria*

[3]*University of Vienna Research Platform MMM Mathematics - Magnetism - Materials, University of Vienna, Vienna, Austria*

(Received 18 February 2021; revised 14 October 2021; accepted 14 October 2021; published 25 October 2021)

We explored the variations of the topological magnetic textures of vortices, skyrmions, and skyrmioniums in magnetic elements of hemispherical-shell shape with respect to surface-normal uniaxial magnetic anisotropy constant K_u, Dzyaloshinskii-Moriya interaction (DMI) constant D_{int}, and shell diameter $2R$. For given values of $2R$, the combination of K_u and D_{int} plays a crucial role in the stabilization of those different spin textures. With decreasing $2R$, the geometrical confinement of hemispherical shells more significantly affects the stabilization of skyrmions owing to curvature-induced DM-like interaction. This effect is contrastingly dependent on the sign of D_{int}: skyrmion formation is more favorable for positive D_{int} values, whereas it is less favorable for negative ones. A quite promising feature is that skyrmions can be stabilized even in the absence of intrinsic DMI for $2R < 25$ nm. We also explored characteristic dynamic properties of skyrmions excited by in-plane and out-of-plane oscillating magnetic fields. Similarly to the fundamental dynamic modes found in planar dots, in-plane gyration and azimuthal spin-wave modes as well as out-of-plane breathing modes were found, but additional higher-frequency hybrid modes also appeared due to coupling between radially quantized and azimuthal spin-wave modes. Finally, we found a switching behavior of skyrmion polarity through a transient skyrmionium state using very-low-strength AC magnetic fields. This work provides further physical insight into the static and dynamic properties of skyrmions in curved-geometry nanodots and suggests potential applications to low-power-consumption and ultra-high-density information-storage devices.

DOI: 10.1103/PhysRevB.104.134427

I. INTRODUCTION

Topological solitons of magnetic materials such as vortices [1,2], skyrmions [3–5], and skyrmioniums [6–8] have attracted considerable attention [9–11] due to their fundamental characteristics and technological applications to future potential information-storage and -processing devices [12–16]. Earlier studies demonstrated that skyrmions, given advantages including their nanoscale size, topologically protected dynamic behaviors, and ultralow-power-consumption motions, can be used as information carriers [12–16]. These studies focused on two-dimensional (2D) planar nanostructures including nanostripes [12,13], nanodisks [13], and thin films [14–16]. In such 2D planar geometry systems, skyrmion-core gyrations [17,18] and azimuthal spin-wave modes [19,20] in either the clockwise (CW) or counterclockwise (CCW) rotation sense, as excited by in-plane AC magnetic fields, as well as the breathing mode [21] excited by out-of-plane AC magnetic fields, have been found. Among those dynamic features, low-power-consumption motions of tiny skyrmions have attracted much attention, because they can be used as information carriers in racetrack stripes. Furthermore, the skyrmion polarity (defined by either core magnetization) can be switched by different means: magnetic field [22–24], electric field [25,26], or spin current [27,28]. These methods can affect the stability of skyrmions during the modes' excitations. Therefore, it is necessary to sustain transformed states [22–24] or to further enhance the stability of skyrmions, even under continuous AC fields or currents.

In typical 2D planar dots, skyrmion formation generally is stabilized by the competition between the Heisenberg exchange coupling and Dzyaloshinskii-Moriya interaction (DMI) [29,30]. In B20 compounds such as MnSi [31] and FeGe [32], intrinsic bulk DMI arising from a noncentrosymmetric crystalline structure plays a primary role in stabilizing 2D hexagonal lattices of Bloch-type skyrmions [33–34]. In the thin films of interfaces between ferromagnets and heavy metals with strong spin-orbit coupling, interfacial DMI arising from inversion asymmetry at the interfaces plays a dominant role in stabilizing Néel-type skyrmions [35,36]. Quite interestingly, as an alternative route to further stabilization of chiral skyrmions, geometrical confinements have been used to introduce curvature-induced DM-like interaction [37–42]. For example, it was reported that the presence of a localized curvilinear defect enhances the stability of skyrmions in perpendicularly magnetized ferromagnetic thin films, [37,38] and that curvilinear geometries can enhance the effect of DM-like interaction and reduce the effective magnetic anisotropy [40,41]. More promisingly, the curvature effects of spherical

*Corresponding author: sangkoog@snu.ac.kr

shells [39] and hemispherical shells [42] have been reported to further stabilize skyrmions even in the absence of intrinsic DMI. Although these studies reported that skyrmions can be formed more favorably in curved geometries than in 2D planar ones, the dynamic features of spin textures in three-dimensional (3D) nanodots are still lacking, especially in terms of the fundamental modes and their polarity switching for information-storage applications.

In this study, we numerically simulated topologically protected spin textures in a curved geometry of hemispherical shells of 1 nm thickness and $2R = 25$–100 nm diameter with respect to surface-normal uniaxial magnetic anisotropy constant K_u and DMI constant D_{int}. We also explored the characteristic dynamic modes of skyrmions in the model system and found a mechanism of skyrmion polarity switching. The results provide not only a deeper understanding of skyrmion stability in curved geometries but also an efficient means of stabilizing skyrmions in nm-size dots without intrinsic DMI. Furthermore, from an application point of view, such a switching mechanism and further-stabilized skyrmions in the shell structure in the absence of intrinsic DMI are promisingly applicable to low-power-consumption, high-density, nonvolatile memory devices [43].

The paper is organized as follows. Section II details micromagnetic simulations performed for a half-spherical shell model. Section III A discusses a phase diagram of static spin textures along with their topological charges as functions of both K_u and D_{int} constants. Sections III B and III C explain the structure stabilization of Néel-type skyrmions formed in hemispherical shells and their characteristic dynamic modes, respectively. In Secs. III D and III E, the skyrmion polarity switching mechanism is discussed. Finally, in Sec. IV, the results are summarized.

II. MICROMAGNETIC SIMULATIONS

The model employed in the present simulation is a hemispherical shell structure of ultrathin thickness ($t = 1$ nm) representative of different outer diameters ranging 25–100 nm, as shown in Fig. 1(a). In order to examine the dependence of the perpendicular magnetic anisotropy (PMA) on the thickness of thin films [44], we also varied the uniaxial magnetic anisotropy constant K_u, even for a constant single value of shell thickness $t = 1$ nm. The 3D volume of the model structure is discretized into tetrahedrons with an average surface-node distance of 1 nm, and the curved surface is discretized into triangles of nearly equal areas using hierarchical triangular mesh [45] in order to prevent incurring of numerical errors by irregularities. To initially position the core of a single skyrmion at the center, the height (h) was set to 99.9% of a given radius (R) [46]. This geometrical asymmetry does not modify the overall static and dynamic characteristics of a single skyrmion in the shell.

In order to calculate the dynamic motions of individual magnetizations at every node in the given hemispherical shells, micromagnetic simulations were conducted using an internally developed micromagnetic code (magnum.fe) [47] that utilizes the Landau-Lifshitz-Gilbert (LLG) equation [48], $\partial\mathbf{M}/\partial t = -\gamma\mathbf{M}\times\mathbf{H}_{\text{eff}} + (\alpha/M_s)\mathbf{M}\times\partial\mathbf{M}/\partial t$, where α is the Gilbert damping constant, γ is the gyromagnetic ratio, and

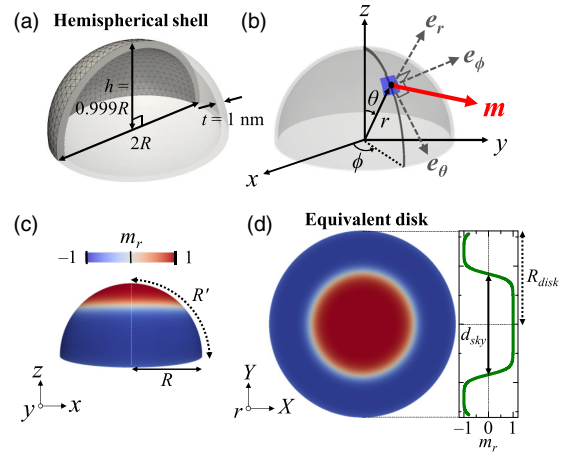

FIG. 1. (a) Perspective view of model system: Hemispherical shell of diameter $2R$, height $h = 0.999R$, and shell thickness $t = 1$ nm. (b) Representation of spherical coordinates of three unit vectors of e_r, e_θ, and e_φ on reference frame of local surface marked by blue surface point for local magnetization m marked by red arrow). (c) Single Néel-type skyrmion in hemispherical shell of $2R = 100$ nm and (d) its unrolled plane-view representation along with corresponding m_r profiles across center of equivalent flat disk. The colors correspond to the surface-normal magnetization component $m_r = M_r/M_s$ as indicated by the scale bar.

$\boldsymbol{H}_{\text{eff}}$ is the effective field given as $\mathbf{H}_{\text{eff}} = -\frac{1}{\mu_0}\frac{\partial E_{\text{tot}}}{\partial \mathbf{M}}$. The total energy density E_{tot} includes the magnetostatic, magnetocrystalline anisotropy, exchange, DMI, and Zeeman energies. The intrinsic DMI energy was employed in the form $E_{\text{DMI}} = \int D_{\text{int}}[\mathbf{m}\cdot\nabla m_n - m_n\nabla\mathbf{m}]\,dV$, where D_{int} is the DMI constant and m_n is the surface-normal component of the magnetization vector field. The materials of the model are assumed to be cobalt (Co) interfaced with platinum (Pt) for the following material parameters [15]: saturation magnetization $M_s = 580\,\text{kA/m}$, exchange stiffness $A_{\text{ex}} = 15\,\text{pJ/m}$, and damping constant $\alpha = 0.3$. In order to examine the variation of static spin textures in hemispherical shells of given diameters with both K_u and D_{int},we varied K_u in a range of $0 \sim 0.8\,\text{MJ/m}^3$ and D_{int} in a range of $-8.0 \sim +8.0\,\text{mJ/m}^2$. The easy axis of magnetic anisotropy as well as the DMI axis were set along the surface-normal axis at each node's position of given shells.

For better visualization of the spin textures obtained in the shells of a curved surface and the radial and azimuthal symmetries, we converted simulation data sets from the Cartesian coordinates (x, y, z) basis to spherical coordinates $(e_r, e_\theta, e_\varphi)$ $(e_r,\ e_\theta,\ e_\varphi)$. As seen in Fig. 1(b), the unit vector of local magnetizations (red arrow) is expressed as $(m_r, m_\theta, m_\varphi) = (\mathbf{m}\cdot\mathbf{e_r}, \mathbf{m}\cdot\mathbf{e}_\theta, \mathbf{m}\cdot\mathbf{e}_\varphi)$, where r is the radial distance, θ is the polar angle, and φ is the azimuthal angle in the frame of local spherical coordinates. Figure 1(c) shows a single skyrmion formed in a hemispherical shell of $2R = 100$ nm and $t = 1$ nm for $K_u = 0.80\,\text{MJ/m}^3$ and $D_{\text{int}} = 3.0\,\text{mJ/m}^2$. For better visualization of the formed skyrmion, Fig. 1(d) shows the 3D shell model unrolled in a planar view according to the following transformation: $X = \frac{\theta}{\sin\theta}x$, $Y = \frac{\theta}{\sin\theta}y$, and $R' = \frac{\pi}{2}R$, where (X, Y) is the in-plane position in

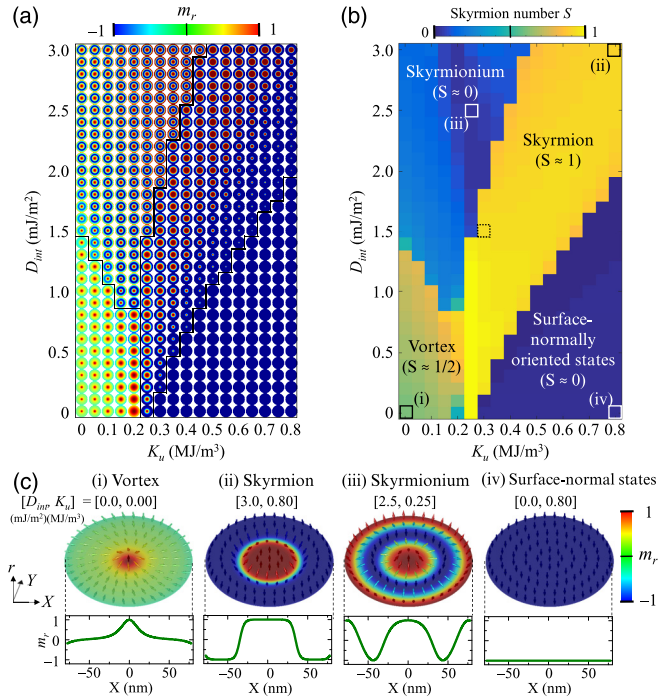

FIG. 2. Phase diagram of different spin textures as functions of surface-normal uniaxial magnetic anisotropy K_u and intrinsic DMI constant D_{int}, as represented by (a) spatial distribution of m_r and (b) topological skyrmion number S. (c) Representative ground (or metastable) states for indicated values of D_{int} and K_u: (i) vortex, (ii) skyrmion, (iii) skyrmionium, and (iv) surface-normal-oriented state along with corresponding m_r profiles across center of hemispherical shell.

the unrolled disk and R' is its radius in the frame of Cartesian coordinates. Note that the spatial distributions of local magnetizations and topological charges in the static and dynamic configurations of spin textures are viewed in such unrolled planar disks (for more details, see Supplemental Material S1 [49]).

III. RESULTS AND DISCUSSION

A. Phase diagram of spin textures

Since uniaxial magnetic anisotropy favors collinear magnetizations while intrinsic DMI prefers noncollinear chiral magnetizations, their competition results in a rich variety of chiral spin textures. We obtained ground-state (or metastable-state) spin textures after relaxation of an intended Néel-type skyrmion state for 10 ns with $\alpha = 1$ in a hemispherical shell of $2R = 100$ nm for $M_s = 580$ kA/m and $A_{\text{ex}} = 15$ pJ/m, with respect to D_{int} in a range 0–3.0 mJ/m^2 in steps of 0.1 mJ/m^2, and K_u in a range 0–0.8 MJ/m^3 in steps of 0.05 MJ/m^3 (for the other shell diameters, see Supplemental Material S2 [49]). Figures 2(a) and 2(b) show the phase diagrams for each set of (K_u, D_{int}), as represented by the spatial distributions of the surface-normal component $m_r = Mr/Ms$ in the unrolled disk and by the corresponding skyrmion number S, respectively, where $S = \iint_A (1/4\pi)\boldsymbol{m} \cdot (\partial_X \boldsymbol{m} \times \partial_Y \boldsymbol{m}) dX dY$ with A representing the entire area of the unrolled disk [50]. In both phase diagrams, the characteristic spin textures are very distinct: vortex, skyrmion, skyrmionium, and surface-normal-oriented magnetization states, as clearly seen in Fig. 2(c). The topological textures of the vortex, skyrmion, and skyrmionium were clrealy classified by their own characteristic magnetization configurations and, furthermore, by the relevant skyrmion number, $S \sim 0.5$ (green), ~ 1 (yellow), and ~ 0 (light blue), respectively [see Fig. 2(b)]. Note that S for the skyrmion state in infinite planar thin films is a unity, but in the shells, the estimated S values are not unity but rather close to 1, due to DMI-induced chiral magnetizations at the boundary of the finite geometry [51]. Figure 2(c) clearly displays the four different characteristic spin textures at [D_{int}(mJ/m^2), K_u(MJ/m^3)] = [0.0, 0.00], [3.0, 0.80], [2.5, 0.25], and [0.0, 0.80], as marked by numbers (i) (vortex), (ii) (skyrmion), (iii) (skyrmionium), and (iv) (surface-normal-oriented states), respectively, on the phase diagram. The directions of the arrows and local colors represent the directions of the local magnetizations and their surface-normal components (m_r), respectively. The corresponding line profiles of m_r across the geometrical center of the shells feature the representative magnetization configurations of the vortex, skyrmion, skyrmionium, and surface-normal states.

For lower K_u and D_{int} values (left-bottom corner region in phase diagram), the vortex states are favorable, which consist of out-of-plane magnetizations at the core and in-plane magnetizations radially pointing to the core. The radial vortex structure is known to appear in planar disks as well in cases where interfacial DMI is employed [52]. The size of the vortex core increases with K_u for given values of D_{int} [see Fig. 2(a)]. On the other hand, for K_u values larger than a certain critical value of K_u as well as D_{int} values marked by the yellow regions in Fig. 2(b), the skyrmion states are stabilized. The skyrmion state is characterized by upward (or downward) magnetizations at the core along with opposite core magnetizations around the core, as well as the Néel-type domain wall between the two regions. The size of the skyrmion core increases with D_{int} but decreases with K_u up to its threshold value above which the skyrmion state transforms into the surface-normal-oriented state.

We should note that even with zero D_{int}, the skyrmion state appeared at $K_u = 0.25$ MJ/m^3, which was caused by the curvature-induced DM-like interaction [40,41]. Furthermore, quite interestingly, skyrmionium states appeared in a certain region (left top) of higher D_{int} and lower K_u values, which differ from both the vortex and skyrmion states [see (iii) of Fig. 2(c)]. The skyrmionium state shows additional upward magnetizations at the edge compared to the skyrmion structure. In addition, the in-plane magnetizations in the inner and outer domain walls point towards the core and the edge, respectively, and this structure is called the skyrmionium state (2π-skyrmion) [53,54]. Finally, in a region of higher K_u and lower D_{int} values (right-bottom corner), there exist surface-normal magnetization states at every local surface of the hemispherical shell, because the higher uniaxial anisotropy prefers collinear magnetization overcoming the lower DMI that prefers chiral magnetizations. Note that the skyrmion number for both the skyrmionium and surface-normal magnetization states is $S \sim 0$, whereas the two spin textures are totally different.

B. Static structure of skyrmion in hemispherical shells

It is known that the sign of $D_{\rm int}$ determines either left- or right-handed helicity in the planar geometries [55], and that the magnitude of $D_{\rm int}$ governs the core size of a skyrmion. In this regard, the effects of the sign and magnitude of $D_{\rm int}$ on the static skyrmion structure in the hemispherical shells were investigated based on numerical calculations of skyrmions for both positive and negative signs of $D_{\rm int}$ as well as its magnitude. The positive (negative) sign of $D_{\rm int}$ represents the outward (inward) DMI axis in the given convex curvature of shells. In order to examine the curvature effect on the formation of skyrmions, we estimated the core size of skyrmions as a function of $D_{\rm int}$ in a range of -8.0 to $+8.0\,{\rm mJ/m^2}$ at a fixed value of $K_u = 0.80\,{\rm MJ/m^3}$ as an example, for different shell diameters of $2R = 25$, 50, and 100 nm. For the sake of convenience in the analysis, we defined the core size of skyrmions as $d_{\rm sky}$ using the zero surface-normal magnetization (i.e., $m_r = 0$), as shown in Fig. 1(d).

For a clear comparison, we also calculated the $d_{\rm sky}$ vs $D_{\rm int}$ curves for both the negative and positive values of $D_{\rm int}$ for a 2D circular disk of diameter $2R_{\rm disk} = 157$ nm, whose diameter is equivalent to $2R = 100$ nm in the 3D hemispherical shell [see Fig. 3(a)]. The $d_{\rm sky}$-vs-$D_{\rm int}$ curves (black square symbols) are symmetric about $D_{\rm int} = 0$ for the 2D planar geometry, but asymmetric for the 3D shells, and become much more asymmetric with smaller diameters $2R$. Such asymmetric behaviors of the $d_{\rm sky}$ vs $D_{\rm int}$ curves for the positive and negative signs of $D_{\rm int}$ are curvature-induced DM-like interactions, as reported in Refs. [40,41], which appears to be an effective term for the exchange interaction (see Supplemental Material S3 [49] for details).

In detail, the core size of skyrmions increases with increasing $|D_{\rm int}|$, whether the sign of $D_{\rm int}$ is negative or positive. For smaller $D_{\rm int}$ values less than certain critical values, $D_{\rm th}$ (denoted by corresponding open symbols), the core size of skyrmions cannot be defined due to the fact that the skyrmions are energetically unstable, and thus no longer exist [56,57]. With increasing $|D_{\rm int}|$ $|D_{\rm int}|$, the rate of increase of $d_{\rm sky}$ is reduced, reaching its maximum core size. Note that the $D_{\rm th}$ values are quite different for the positive and negative signs of $D_{\rm int}$ for the indicated $2R$ values. For example, for $2R = 100$ nm, $D_{\rm th}$ is 2.0 and $-3.5\,{\rm mJ/m^2}$ for the left- and right-handed skyrmions, respectively. This difference increases with decreasing shell diameter, $2R$. For $D_{\rm int} > 0$, the $|D_{\rm th}|$ values decrease with decreasing $2R$, while $|D_{\rm th}|$ increases markedly with decreasing $2R$ for $D_{\rm int} < 0$. For smaller $2R$, the variation of $d_{\rm sky}$ is not as large as for the larger $2R$, because the shell diameter limits the size of skyrmions as well. Those results indicate the fact that for the left-handed helicity ($D_{\rm int} > 0$), the curvature of the shells facilitates the preferred formation of skyrmions, while for the right-handed helicity ($D_{\rm int} > 0$), the curvature prevents the stable formation of skyrmions. For example, for the $2R = 25$ nm shell, the left-handed skyrmion was stably formed at $D_{\rm int} = 0$ even without intrinsic DMI, and moreover, the skyrmions appeared in a certain region of $D_{\rm int} < 0$ [see the green symbols in Fig. 3(a)].

Such a large discrepancy in $D_{\rm th}$ between the left- and right-handed helicities originates from the curvature of shells. The curvature effect is well presented by the curvature-dependent $D_{\rm th}$ for both the left- and right-handed skyrmions [58]. Linear fits to the simulation data (open symbols) yield $D_{\rm th} = -34.6\,\kappa + 2.59$ for left-handed skyrmions and $D_{\rm th} = -44.5\,\kappa - 2.50$ in a unit of ${\rm mJ/m^2}$ for right-handed skyrmions where κ (${\rm nm^{-1}}$) is the curvature as defined by the reciprocal of the radius ($1/R$). $\kappa = 0$ corresponds to surface-flat disks, and thus $D_{\rm th}$ ($\kappa = 0$) $= +2.59$ and $-2.50\,{\rm mJ/m^2}$ for the left- and right-handed helicities corresponding to the DMI values required for skyrmion formation in planar geometry. The values are close to $|D_{\rm int}| = 3.0\,{\rm mJ/m^2}$ (for the 2D planar geometry) measured for real Co/Pt films [13]. On the other hand, as the curvature increases, $D_{\rm th}$ decreases. This again clearly evidences that the curvature affects the stability of skyrmion formation via curvature-induced DM-like interaction. For the left-handed skyrmion, the $D_{\rm th}$ magnitude required for skyrmion formation decreases with the curvature until crossing zero, indicating greater stability. On the other hand, for the right-handed skyrmion, the $D_{\rm th}$ magnitude increases

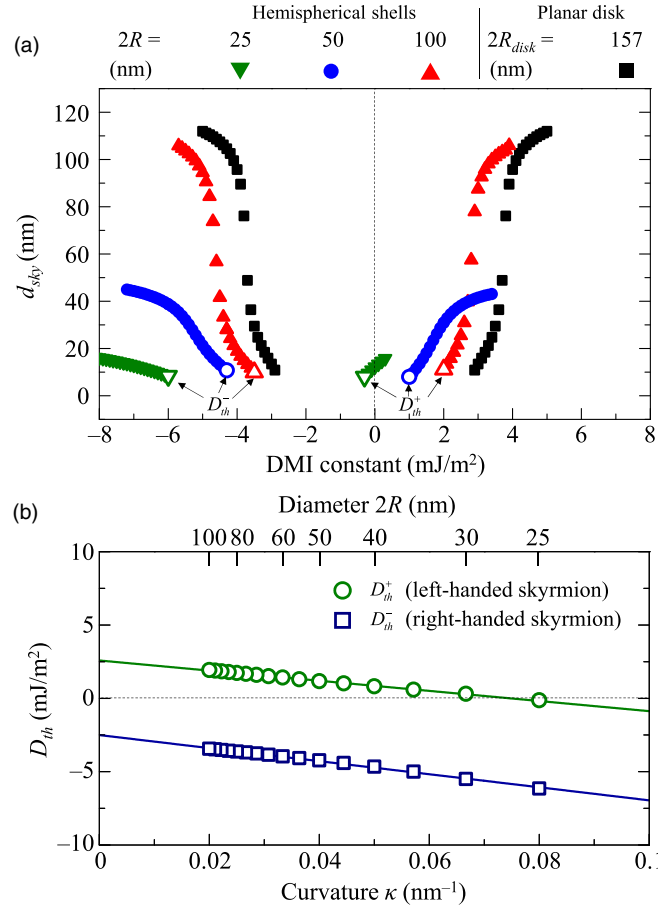

FIG. 3. (a) Size ($d_{\rm sky}$) of skyrmions formed in shells of indicated diameter (here $2R = 25$, 50, 100 as examples) as a function of intrinsic DMI constant $D_{\rm int}$. In this plot, $d_{\rm sky}$ is the size defined at both $m_r = 0$ points in the unrolled view shown in Fig. 1(d). The open symbols at the smallest $|D_{\rm int}|$ value for each $2R$ represent the threshold DMI constant $|D_{\rm th}|$ below which skyrmions are no longer stable enough to form. (b) $D_{\rm th}^+$ and $D_{\rm th}^-$ versus curvature ($\kappa = 1/R$) of shells for left (open circles)- and right (open squares)-handed skyrmions. The solid lines represent the results of linear fitting to the data (open symbols) using a least-square method.

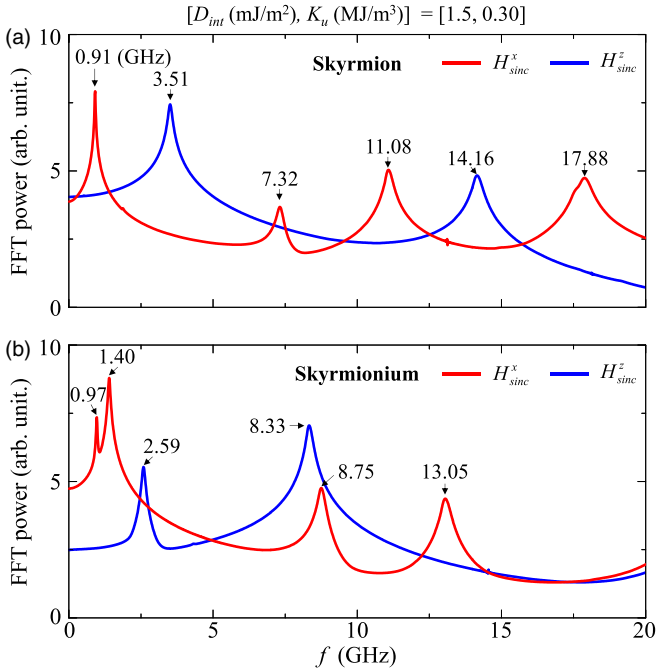

FIG. 4. FFT power spectra averaged over entire area of given hemispherical shell having (a) single skyrmion and (b) skyrmionium, as obtained from FFTs of temporal oscillations of m_r at all individual nodes, as excited by each of sinc fields applied along x (red), and z (blue) axes.

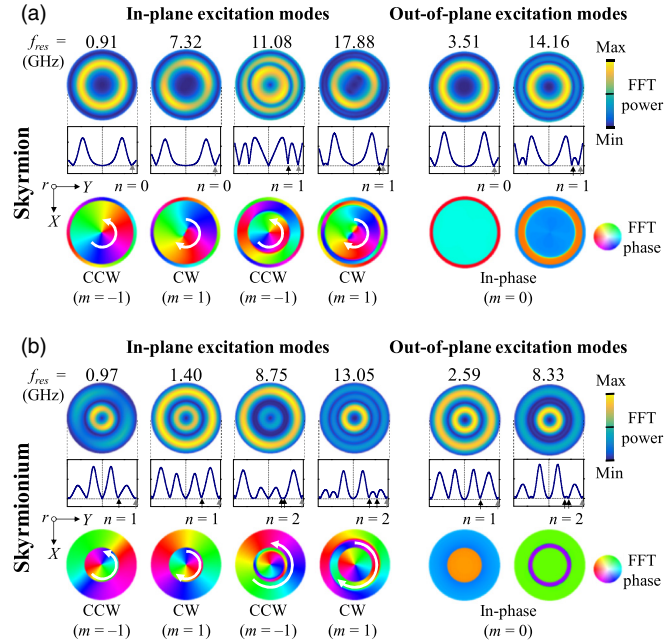

FIG. 5. Unrolled (plane)-view images of spatial distributions of FFT powers along with corresponding line profiles across center position (top) and FFT phase (bottom) obtained at individual resonance frequencies of in-plane and out-of-plane excitations for (a) skyrmion and (b) skyrmionium states. The white circular arrows in each FFT phase image indicates the rotation sense of each dynamic mode. The n and m indices correspond to the numbers of the radial and azimuthal nodes, respectively.

with the curvature. As reported in Ref. [39], the curved geometry plays another crucial role in the formation of skyrmions, enhancing (suppressing) the stability of skyrmion formation for the left (right)-handed helicity.

C. Dynamic modes in skyrmion and skyrmionium states

We addressed the variation of static spin textures according to $D_{\rm int}$, K_u, and $2R$. Based on the observed skyrmion and skyrmionium states, we also explored their dynamic modes for $2R = 100\,$nm, as a representative example, for $(D_{\rm int}, K_u) = (1.5\,{\rm mJ/m^2}, 0.30\,{\rm MJ/m^3})$ at a point indicated by the black dashed-line square in Fig. 2(b). Under the same condition, the skyrmionium state is metastable, which energy ($-1.0\times10^{-18}\,$J) is higher than that ($-1.1\times10^{-18}\,$J) of the skyrmion. To the given skyrmion and skyrmionium states, we applied a sinc-function field $\mathbf{H}_{\sin c}(t) = \mathbf{H}_0 \sin[2\pi f_{\rm H}(t - t_0)]/[2\pi f_{\rm H}(t - t_0)]$ with $|\mathbf{H}_0| = 10\,$Oe, $f_{\rm H} = 100\,$GHz, $t_0 = 1\,$ns, and $t = 100\,$ns along each of the x and z axes, whose axes correspond to the in-plane and out-of-plane directions with respect to the shell center, respectively. In order to obtain a better spectral resolution for appropriate interpretation and analysis of the spin-wave modes, we used a constant damping parameter of $\alpha = 0.01$ instead of its actual value ($\sim$0.3 for Co/Pt) [13]. Note that the smaller damping constant affects the width and magnitude of the mode peaks, but not their peak positions [59,60]. Figures 4(a) and 4(b) show the resultant spectra of all of the excited modes, as obtained from the averaged fast Fourier transforms (FFTs) of the m_r oscillations at the individual nodes in the total volume of the half-spherical shell for the skyrmion and skyrmionium states, respectively.

For the skyrmion, four modes were excited at 0.91, 7.32, 11.08, and 17.88 GHz by the in-plane field excitation (red color), and two modes were excited at 3.51 and 17.88 GHz by the out-of-plane field excitation (blue color). For the skyrmionium, although the frequency positions were different from those for the skyrmions, the same numbers of excited modes were observed: four modes at 0.97, 1.40, 8.75, and 13.05 GHz by the in-plane field (red color), and two modes at 2.59 and 8.33 GHz by the out-of-plane field (blue color). Note that the strongest modes for the skyrmion are at the lowest frequency, i.e., 0.91 GHz for the in-plane field and 3.51 GHz for the out-of-plane field. On the other hand, the strongest modes for the skyrmionium are at the second-lowest frequency, i.e., 1.40 GHz for the in-plane field and 8.33 GHz for the out-of-plane field.

In order to identify all of the excited modes shown in the spectra (Fig. 4), we plotted the spatial distributions of the FFT power (top) and phase (bottom) at the indicated resonance frequencies, as shown in each of Figs. 5(a) and 5(b). The power line profiles across the geometrical center along the radial axis clearly exhibit the position and number of radial nodes n, as denoted by small black arrows in the profiles, while the phase distributions represent the azimuthal nodes m. We note that one single node near the edge of each shell (indicated by gray arrows) was excluded from the numbering of the radial node n, because the node was not generated by the excitation of the real eigenmodes, but rather by the edge-boundary effect of the already-noted curvature-induced DM-like interaction.

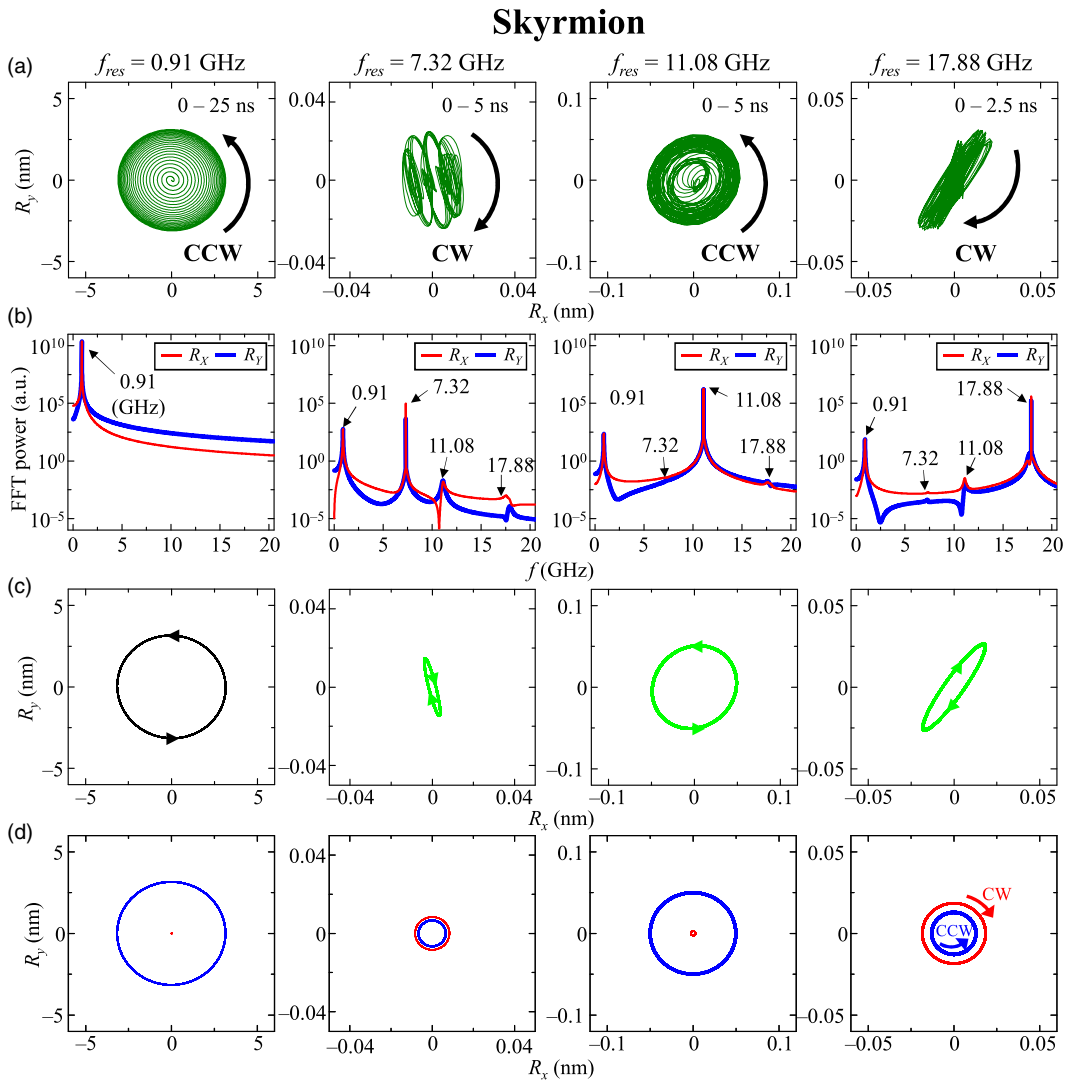

FIG. 6. (a) Trajectories of core in-plane motions represented by guiding center of skyrmion in indicated time ranges for each of $f_{\rm res} = 0.91$, 7.32, 11.08, and 17.88 GHz resonant excitations. (b) FFT-power spectra obtained from FFTs of X (red) and Y (blue) components of guiding center shown in Fig. 6(a). (c) Frequency-selective core trajectories: first, second, third, and fourth panels were obtained from inverse FFTs from FFT powers at $f_{\rm res} = 0.91$, 7.32, 11.08, and 17.88 GHz, respectively. (d) CCW (blue) and CW (red) circular core trajectories decomposed from elliptical core trajectories shown in (c).

As for the skyrmionium, the number of radial nodes n is always one more than those of the skyrmion, because the skyrmionium consists of two inner and outer skyrmion states, and between the two, there exists an additional circular domain wall that acts as a node. Accordingly, the excited modes of the skyrmion and skyrmionium states can be indexed by both the radial and azimuthal symmetry characterized nodes, n and m, respectively, as shown in Fig. 5. For the in-plane field excitation, the two lower (higher)-frequency modes correspond to $n = 0$ (1) and $n = 1$ (2) for the skyrmion and skyrmionium states, respectively. For each of $n = 0$, 1, and 2, there exists a phase change from $-\pi$ to π or vice versa, in either the CCW ($m = -1$) or CW ($m = 1$) rotation sense. For the out-of-plane field excitation, the radial node numbers of the lower- and higher-frequency breathing modes are $n = 0$ and 1, respectively, for the skyrmion, and $n = 1$ and 2 for the skyrmionium. The azimuthal node is $m = 0$, corresponding to the in-phase in the azimuthal direction.

The above-noted modes appeared to be similar to those found by Mruczkiewicz *et al.* [19,20], who classified the excited modes of skyrmions in 2D planar disks as gyration, azimuthal, and breathing modes. In our work, to further elucidate the dynamic modes of both the skyrmion and skyrmionium states, we extracted the trajectories of the core motions of the skyrmion and skyrmionium under applications of each of the single-resonance frequencies of the individual in-plane modes (see Supplemental Material S4 [49] for the detailed dynamic motions). Figure 6(a) shows the resultant core trajectories, plotting the guiding center $\mathbf{X} = (R_x, R_y)$, where $R_x = \int xqdxdy / \int qdxdy$ and $R_y = \int yqdxdy / \int qdxdy$ with the topological charge density $q = (1/4\pi)\mathbf{m} \cdot (\partial_x \mathbf{m} \times \partial_y \mathbf{m})$ [50]. For the 0.91 GHz mode, the skyrmion core exhibits a large-amplitude circular gyration motion in the CCW rotation for the upward core magnetization. For the other modes of 7.32, 11.08, and 17.88 GHz, the core trajectories show rather complicated elliptical motions. It is certain that the 0.91-GHz

motion is the gyrotropic mode of the skyrmion with an orbit radius of ∼3.14 nm. Contrastingly, the core motions at 7.32, 11.08, and 17.88 GHz present orbit radii as small as ∼0.015, ∼0.054, and 0.022 nm, respectively. In addition, the rotation senses of the 7.32- and 17.88-GHz modes are opposite to the CCW motion of the first gyration mode, i.e., CW, even for the upward core magnetization. Thus, the in-plane core motions for the higher-frequency modes are associated with coupling with the azimuthal spin-wave modes [19,20], as shown in Fig. 4(a).

In order to further interpret the complicated core motions of the higher-frequency modes, we conducted FFTs of the temporal variations of the X and Y components of the core position shown in Fig. 6(a). The resultant FFT power spectra in the frequency domain are given in Fig. 6(b). For the 0.91-GHz mode, the power spectrum shows only a strong single peak at 0.91 GHz. Surprisingly, for each of 7.32-, 11.08-, and 17.88-GHz modes, all of the peaks appeared at the same resonance frequencies as those of the already noted four modes. The strongest peak in each case appeared at the corresponding frequencies of the applied AC fields. This means that for the higher-frequency modes, small peaks around the corresponding main peak were excited by the coupling of the core with the azimuthal spin-wave modes. The azimuthal mode splitting into the CW ($m < 0$) and CCW ($m > 0$) modes is known to be typical for a single skyrmion in a planar nanodisk system [20], owing to DMI-induced spin-wave nonreciprocity. Thus, these complex core motions for the 7.32-, 11.08-, and 17.88-GHz modes were the result of the hybridization between the core and the azimuthal spin-wave eigenmodes of 7.32, 11.08, and 17.88 GHz as well as the strong gyrotropic mode of 0.91 GHz. These complex core motions are also similar to the dynamic behaviors of a single vortex core interacting with propagating spin waves, as reported in Refs. [61,62].

From the spectra plotted in Fig. 6(b), we also conducted inverse FFTs of the strongest peak for each resonance excitation to obtain frequency-selective core trajectories from the complicated core trajectories shown in Fig. 6(a). In Fig. 6(c), the 0.91-GHz peak exhibits a CCW circular motion (black curves), while each of the 7.32-, 11.08-, and 17.88-GHz peaks represents an elliptical core trajectory of a different ellipticity (green curve). It is known that the elliptical core trajectory of gyration modes can be interpreted as the superposition of the clockwise (CW) and counterclockwise (CCW) circular gyration eigenmodes [63]. Thus, the elliptical core trajectories (green curves) can be decomposed into the orthogonal CCW (blue) and CW (red) circular eigenmodes, as shown in Fig. 6(d). The relative magnitudes of the phase and the radius amplitude between the CCW and CW circular eigenmodes yield contrasting rotation angles and ellipticities, respectively [63] [cf. Figs. 6(c) and 6(d)]. Thus, from the elliptical core trajectories shown in Fig. 6(c), we can determine the ellipticity η_G and rotation angle θ_G, as defined by the ratio of the length of the long-to-short axis and the angle of the long axis of the ellipse from the $+Y$ direction, respectively. From the estimation of θ_G and η_G, we also can determine the phase difference and the relative amplitude between the CCW and CW circular modes according to $\delta_{\mathrm{CCW}} - \delta_{\mathrm{CW}} = 2\theta_G$ and $|X_{\mathrm{CCW}}|/|X_{\mathrm{CW}}| = (1+\eta_G)/(1-\eta_G)$ [64], where δ and $|X|$ are the phase and amplitude of the core motion for each of the CCW and CW circular modes. These estimated parameters of the elliptical core motions are summarized in Table I. For the 0.91- and 11.08-GHz modes in Fig. 6(c), η_G is estimated to be 1.02 and 1.12, respectively, indicating nearly circular trajectories of core rotation in the CCW rotation sense. The CCW rotation sense of the core trajectory is caused by the gyrotropic force of the upward core orientation [17,18], as indicated by the large values of $|X_{\mathrm{CCW}}|/|X_{\mathrm{CW}}|$, being 120.6 (0.91 GHz) and 18.28 (11.08 GHz). In contrast, the core trajectories for the 7.32- and 17.88-GHz modes represent considerable elliptical shapes of core motions rotating in the CW rotation sense, as revealed by the large values of $\eta_G = 8.51$ (7.32 GHz) and 5.66 (17.88 GHz). On the other hand, the $|X_{\mathrm{CCW}}|/|X_{\mathrm{CW}}|$ ratios are 0.79 for 7.32 GHz and 0.70 for 17.88 GHz, i.e., less than 1. They indicate that the CW rotation mode is more dominant than the CCW mode [19], even though the two modes are almost equivalent in amplitude. According to the above discussions, the complex elliptical core motions shown in Fig. 6(a) are the result of the superposition of the two circular eigenmodes of core gyrations, which can be also excited by the hybridization of azimuthal spin-wave modes.

TABLE I. Numerical estimation of ellipticity η_G and rotation angle θ_G for skyrmion's core trajectories shown in Fig. 7(c). The phase difference $\delta_{\mathrm{CCW}} - \delta_{\mathrm{CW}}$ and the relative amplitude ratio $|X_{\mathrm{CCW}}|/|X_{\mathrm{CW}}|$ were calculated from both values of η_G and θ_G, and agreed with those obtained from the decomposed CCW and CW circular modes shown in Fig. 7(d).

f_{res}(GHz)	0.91	7.32	11.08	17.88
η_G	1.0	8.5	1.1	5.6
θ_G (°)	43.3	13.5	36.6	−33.9
$\delta_{\mathrm{CCW}} - \delta_{\mathrm{CW}}$ (°)	87	27	73	−68
$\lvert X_{\mathrm{CCW}}\rvert/\lvert X_{\mathrm{CW}}\rvert$	121	0.79	18.3	0.70
$\lvert X_{\mathrm{CCW}}\rvert$ (nm)	3.15	0.0066	0.05	0.013
$\lvert X_{\mathrm{CW}}\rvert$ (nm)	0.026	0.0084	0.003	0.019

Next, we now move on to the dynamic behaviors of a single skyrmionium formed in the hemispherical shell. Figure 7(a) shows the resultant core trajectories obtained from the calculations of the center of mass of the skyrmionium magnetization [65] excited by the application of AC magnetic fields of each of the corresponding resonance frequencies, i.e., 0.97, 1.40, 8.75, and 13.05 GHz. For the two lower-frequency modes of 0.97 and 1.40 GHz, the core trajectories represent large-amplitude (0.33 and 0.52 nm) gyrations in the CCW and CW rotational senses, respectively, whereas for the two higher-frequency modes of 8.75 and 13.05 GHz, they show relatively small-amplitude (0.011 and 0.023 nm) gyrations in the CCW and CW rotational senses, respectively. For a better analysis of such complex core motions of skyrmioniums, we conducted the same analysis steps as those for the skyrmions shown in Figs. 6(a)–6(d). Figure 7(b) shows the FFT power spectra where strong peaks appeared at the corresponding resonance frequencies of applied AC magnetic fields, along with smaller peaks at the resonance frequencies of all of the other modes. Figure 7(c) shows the frequency-selective core trajectories of a skyrmionium conducted by the inverse FFTs

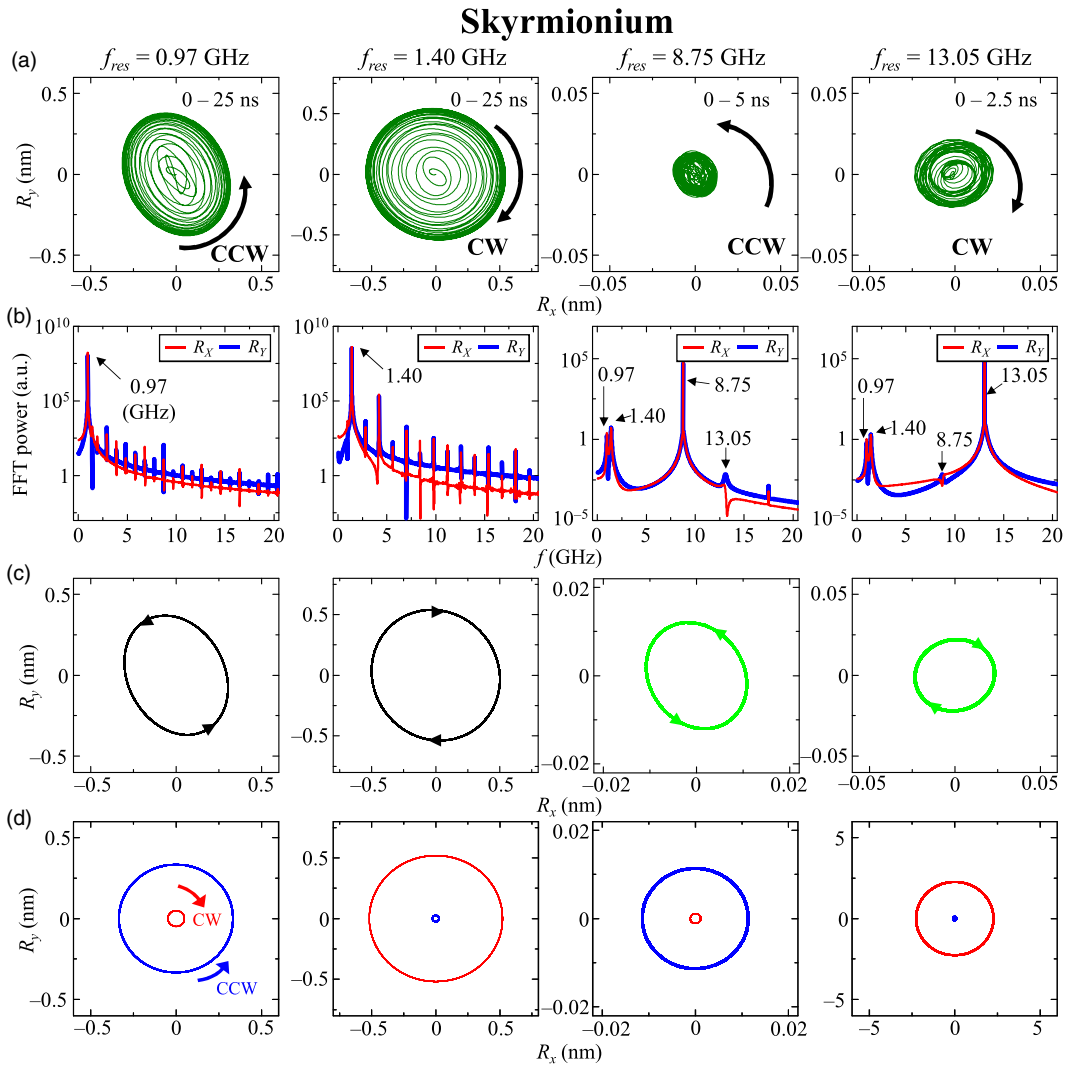

FIG. 7. (a) Trajectories of core in-plane motions represented by the center of mass of the skyrmionium magnetization in indicated time ranges for each of $f_{\text{res}} = 0.97$-, 1.40-, 8.75-, and 13.05-GHz resonant excitations. Panels (b)–(d) were obtained from the same procedures as described in Fig. 6.

of the strongest peak as excited by each resonance-frequency excitation.

The lower-frequency in-plane core motions represent the fundamental gyration modes, because they show almost circular core trajectories with large orbiting radii in the CCW rotation of the upward core and in the CW rotation of the downward outer part of the skyrmionium. By contrast, the higher-frequency in-plane core motions represent relatively very small orbit radii (0.011 and 0.023 nm) in the CCW and CW rotation senses for the 8.75- and 13.05-GHz modes. Although these rotation senses are shown as either CCW or CW as in the gyration modes, the dynamic origins are determined by the azimuthal spin-wave modes, because the higher-frequency core motions are associated with coupling of the core with the azimuthal spin-wave modes [19,20], as evidenced in Fig. 4(b). Similarly to the modes of a single skyrmion, the rotation senses of the core motion for the 8.75- and 13.05-GHz modes are determined by the rotational sense of the azimuthal spin-wave modes through their interaction with the given upward inner core as well as the downward outer part of the skyrmionium (see Fig. 6). This finding is contrary to a previous report [66] that suggested that there are four in-plane gyrotropic spin-wave excitation modes (i.e., two low-frequency modes and two high-frequency modes) for a skyrmionium. In Fig. 7(d), similarly to the case of the skyrmion, the elliptical core trajectories were decomposed into the CCW (red) and CW (blue) circular eigenmodes [63]. Table II also shows the numerical values of η_G and θ_G as estimated from Fig. 7(c). For 0.97 GHz, the ellipticity of $\eta_G = 1.3$ consists of the CCW and CW circular eigenmode amplitudes in the 6.84:1 ratio. This is somewhat complicated, because the skyrmionium consists of two parts, namely inner and outer skyrmions with opposite out-of-plane magnetizations. The CCW rotation sense is influenced by the upward inner core while the CW rotation sense is affected by the downward magnetization in the outer part. In contrast to the 0.97-GHz mode, the 1.40-GHz mode exhibits a nearly circular ($\eta_G = 1.1$) core trajectory that rotates mostly in the CW direction ($|X_{\text{CCW}}|/|X_{\text{CW}}| = 0.048$). This means that the 1.40-GHz mode is mainly influenced by the downward core

TABLE II. Numerical estimation of ellipticity η_G and rotation angle θ_G for skyrmionium's core trajectories shown in Fig. 8(c). The phase difference $\delta_{CCW} - \delta_{CW}$ and the relative amplitude ratio $|X_{CCW}|/|X_{CW}|$ were calculated from both values of η_G and θ_G, and agreed with those obtained from the decomposed CCW and CW circular modes shown in Fig. 8(d).

f_{res}(GHz)	0.97	1.40	8.75	13.05
η_G	1.3	1.1	1.2	1.1
θ_G (°)	23.7	20.8	27.6	−23.1
$\delta_{CCW} - \delta_{CW}$ (°)	46	42	55	−46
$\|X_{CCW}\|/\|X_{CW}\|$	6.84	0.048	10.24	0.038
$\|X_{CCW}\|$ (nm)	0.3337	0.0251	0.0114	8.797×10^{-4}
$\|X_{CW}\|$ (nm)	0.0488	0.5191	0.0011	0.0229

magnetization of the outer part rather than by the upward core magnetization in the inner center. The core trajectories for the 8.75- and 13.05-GHz modes represent elliptical shapes, with $\eta_G = 1.2$ and 1.1, respectively, with the CCW and CW rotation senses, respectively. By decomposing them into the CCW and CW circular eigenmodes, we found that each mode consisted of $|X_{CCW}|/|X_{CW}| = 10.24$ for 8.75 GHz and 0.038 for 13.05 GHz. Since the skyrmionium consists of two parts, the inner skyrmion and opposite outer part, those core in-plane motions are complicated by the dynamics of the eigenmodes excited in the two different parts as well as the hybridization with azimuthal spin-wave modes excited in the two parts. Further studies are necessary for deeper understanding of the characteristic dynamics of skyrmioniums.

D. Transition between skyrmion and skyrmionium states

Earlier, we addressed two different skyrmion and skyrmionium states. Next, we examined their transition by applying specific-resonance AC fields $\mathbf{H}(t) = \mathbf{H}_{AC}\sin(2\pi f_{res}t)$, with f_H the frequency and $\mathbf{H}_{AC} = H_{AC}\hat{\mathbf{z}}$ the amplitude strength along the core axis (z axis), for, as an example, $2R = 100$ nm. Figures 8(a) and 8(c) show the transition from the skyrmion to skyrmionium state and its reverse, respectively. The magnetization configurations represented by the m_r component at the indicated specific times are displayed along with the m_r line profiles across the shell center. The average m_z component over the shell (black), the corresponding skyrmion number S (orange), and the resultant energy (blue) are represented in Figs. 8(b) and 8(d).

The skyrmion of upward core magnetization ($S = +1$) was transformed into a skyrmionium ($S = 0$) of the same upward core by an AC field of $f_H = 3.51$ GHz and $H_{AC} = 9$ mT in a time period of $t = 10$ ns. Upon applying the resonant magnetic field, the skyrmion started to breathe along the z axis via repeated shrinking and expanding of the upward core. Then, finally the downward magnetizations at the edge area of the initial skyrmion state were switched to the upward ones at $t = 10$ ns, resulting in the skyrmionium state of the upward core magnetization. Once the initial skyrmion state ($S = +1$) was transformed into the skyrmionium state ($S = 0$), the resonant frequency (3.51 GHz) to the initial skyrmion state turns out to be an off-resonance frequency to the final skyrmionium state (2.59 GHz). Thus, the transition process is finally terminated

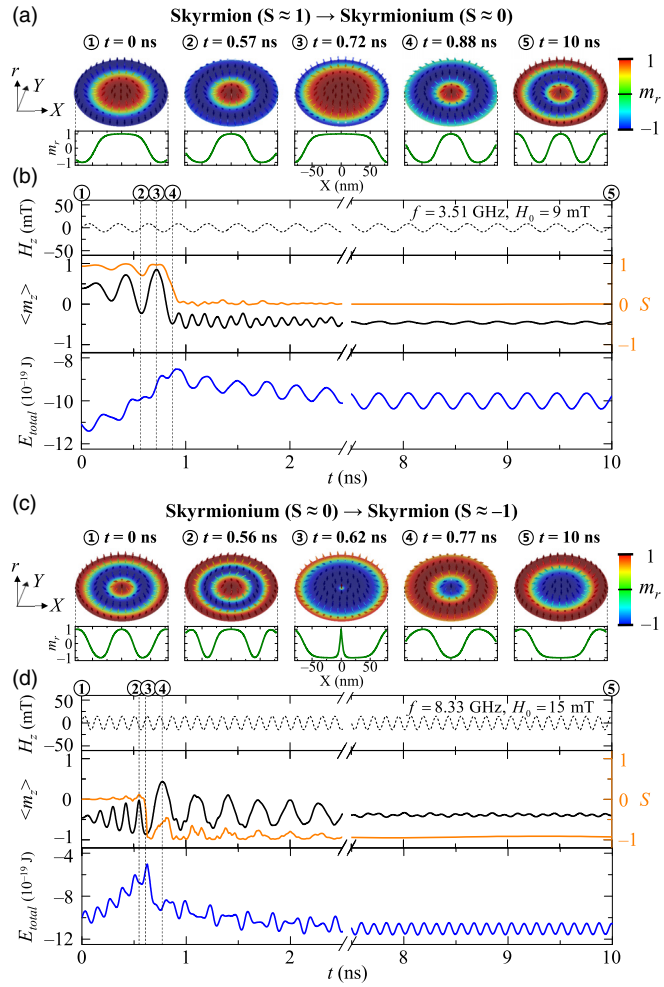

FIG. 8. Panels (a) and (c) represent transition processes from skyrmion to skyrmionium state and skyrmionium to skyrmion state, respectively, as represented by snapshot images (at indicated times) of m_r component distributions along with corresponding line profiles across geometric center. For both of the transition processes, (b) and (d) indicate temporal variations of the H_z component (black dashed line), the $\langle m_z\rangle$ component averaged over the shell (black line), the skyrmion number S (orange line), and the total energy E_{total} (blue line). The black vertical dashed lines correspond to the specific times taken for the snapshot images shown above.

with the skyrmionium state with a slightly damped oscillation of the magnetization. In order to clearly show the transition process of spin textures, we also plotted the values of $\langle m_z\rangle$, S, and E_{total} as a function of time, as shown in Fig. 8(b).

Next, we examined the transition from the initial skyrmionium to the final skyrmion state. Figure 8(c) shows the variation of spin textures during the transition process driven by a different field frequency of $f_H = 8.33$ GHz (corresponding to the resonance frequency of the skyrmionium breathing mode) and $H_{AC} = 15$ mT. Upon application of this pumping field to the skyrmionium state, its higher-order breathing mode ($n = 2$, $m = 0$) was excited, as the inner core expanded ($t = 0.56$ ns) and shrank ($t = 0.62$ ns). Immediately after the inner core was annihilated at $t = 0.62$ ns, the downward magnetization around the core of the initial skyrmionium state was shrunk

in size and finally transformed into another skyrmion with a downward core magnetization ($t = 10$ ns). In contrast to the transition from the skyrmion to the skyrmionium state, where the upward core is maintained during the transition process, the initial upward core is switched to the downward core during the transition from the skyrmionium to skyrmion state [see Fig. 8(c)]. Once the initial skyrmionium state ($S = 0$) is converted to the skyrmion state ($S = -1$), the resonant frequency to the skyrmionium becomes an off-resonance one to the transformed skyrmion state. Thus, no further reverse transition occurs. Thus, this whole process represents a core reversal of the skyrmion state through the skyrmionium transient state. In this core-reversal process, high-frequency spin waves are also radiated from the core through an exchange-energy explosion to dissipate the energy stored at the core, as evidenced by the decay of the $\langle m_z \rangle$ and total energy fluctuation. A movie of the entire transition process is provided in the Supplemental Material Movie 3 [49].

E. Core switching of skyrmion

From an application point of view, these core reversals can be used to switch the core magnetizations of a stable skyrmion state that can be implemented in ultrahigh-density, nonvolatile memory devices since the skyrmion has a topological charge of either $+1$ or -1 depending on the core polarity as topologically protected spin textures. Additional micromagnetic simulations were further conducted to obtain the phase diagram of each of the skyrmion-to-skyrmionium transitions and the reverse case with respect to both H_{AC} and f_{H}, as represented by the skyrmion number S and the time period t_{trans} required for both transitions. In the simulations, we used H_{AC} in a range 0–12 mT (interval: 1 mT) and f_{H} in a range 2–16 GHz (interval: 0.5 GHz) for the skyrmion-to-skyrmionium transition [see Fig. 9(a)] and, for the skyrmionium-to-skyrmion transition, H_{AC} in a range 0–20 mT (interval: 1 mT) and f_{H} in a range 1–10 GHz (interval: 0.5 GHz) [see Fig. 9(b)]. Since $S = +1$ or -1 represents the skyrmion state of either upward or downward core magnetizations whereas $S = 0$ represents a skyrmionium state of either core polarity, the recognition of each state can be monitored by the temporal variation of the skyrmion number S.

At the top of Fig. 9(a), the skyrmion-to-skyrmionium transition occurred in a very specific frequency region at resonance (3.51 GHz, the eigenfrequency of the $n = 0$ breathing modes of the skyrmion) above a certain threshold strength (about 6 mT) of the AC field. At the top of Fig. 9(b), the skyrmionium-to-skyrmion transition occurred at 8.33 GHz, corresponding to the eigenfrequency of the $n = 2$ breathing modes of the skyrmionium, above a different threshold field of 12 mT. Such low-threshold field strengths are one or two orders smaller than those in planar-geometry disks (i.e., ∼245 mT for the skyrmion-to-skyrmionium transition) [24], owing to the assistance of the strong resonant excitation of the breathing mode in the shell, which is a great advantage over the core reversal of spin textures in planar disks. We note that the "x" symbols in the switching region indicate additional multiple switching between the two states, thus the final state could not be determined [67]. This multiple switching was due to the fact that the difference in the resonant

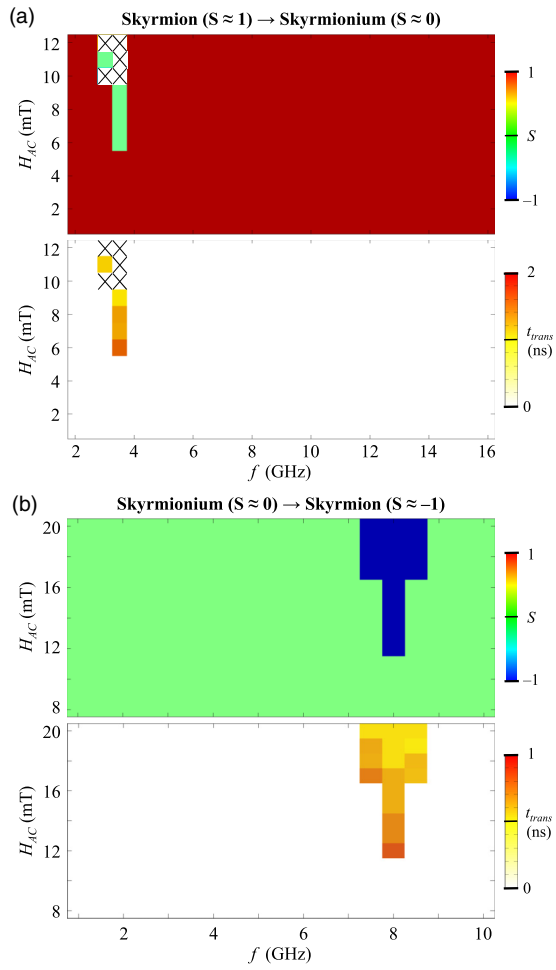

FIG. 9. Phase diagrams of core-reversal (switching) event for (a) skyrmion-to-skyrmionium transition and (b) skyrmionium-to-skyrmion transition. In each of (a) and (b), the skyrmion number S (top) and the switching time (bottom) required to complete each final state are represented on both H_{AC} and f_{H} in the indicated ranges. The red, green, and blue colors in the S phase diagram correspond to the upward core skyrmion, skyrmionium, and downward core skyrmion states, respectively. The "x" symbol represents undermined states due to multiple switching events.

frequencies between the skyrmion and skyrmionium for the first breathing mode (3.51 vs 2.59 GHz) was relatively small. By contrast, in Fig. 9(b), the switching occurred just once and at even higher field strengths than the threshold strength, because the resonant frequencies between the skyrmion and skyrmionium for the second breathing mode were sufficiently large: 14.16 vs 8.33 GHz. As for the time period required to complete switching, the higher the field strength, the faster the switching time in general. The skyrmionium was changed to the skyrmion within a range 0.56–0.97 ns, which is two times faster than for the skyrmion-to-skyrmionium transition (1.13–1.72 ns). These phase diagrams are useful for implementation of such a switching mechanism in real storage devices using highly topologically protected spin textures such as skyrmions and skyrmioniums.

Based on the above results, the core reversal of skyrmions is very promising for potential applications to ultrafast

nonvolatile memory devices, thanks to the following advantages. First, a left-handed skyrmion ($D_{\text{int}} > 0$) on a curved surface of elements of a few nm scale can be stably formed with a smaller DMI constant (or even without intrinsic DMI) than that necessary for a flat surface. Second, either of the skyrmion core polarizations, represented by the binary digit 0 or 1, can be switched ultrafast on the ns time scale. Third, such switching dynamics are readily controllable with externally applied magnetic-field parameters of frequency and strength, and with low power consumption, which would avoid possible joule heating. Fourth and last, with the development of nanofabrication technology [68,69], hemispherical shells and their periodic 2D arrays can be well synthesized on curved-surface dot templates such as spherical polystyrene particles [70,71] and nanoporous alumina membranes [72]. It is also well known that surface-normal-oriented magnetizations can also be established using interfaces between ferromagnetic materials of Co, Ni, and Fe and heavy metals of Pt and Pd, etc. [73–76]. Such layered or multilayer-structured films deposited directly on top of curved-surface dot templates in arrays can form additional curvature-induced stabilized skyrmions [72].

IV. SUMMARY

Using finite-element micromagnetic simulations, we designed magnetic hemispherical shells to further stabilize skyrmions via curvature-induced DM-like interaction and investigated the variation of spin textures with respect to the DMI constant and the surface-normal uniaxial magnetic anisotropy constant. Four different spin textures, those of the vortex, skyrmion, skyrmionium, and surface-normal magnetization states, were found according to the two parameters. Stable formation of single skyrmions was achieved without intrinsic DMI by tuning to the specific values of both parameters. We also examined dynamic modes excited in the skyrmion and skyrmionium states, which modes were classified into lower-frequency gyrotropic modes and higher-frequency spin-wave modes as well as breathing modes. The core in-plane motions and their complicated elliptical core trajectories also were interpreted in terms of the core coupling with azimuthal spin-wave modes. The low-power-consumption switching of core polarity for both skyrmions and skyrmioniums was also found using the breathing-mode-assisted core-magnetization fluctuation. From a fundamental point of view, our work provides a deeper understanding of skyrmion dynamics and their stability in curved geometries. Also, from a technological point of view, with the help of advances in the development of 3D nanostructures as well as high-frequency measurement techniques, the present results offer guidelines for building blocks of skyrmions formed in hemispherical shells for future low-power-consumption, nonvolatile memory devices.

ACKNOWLEDGMENTS

This research was supported by Samsung Electronics Co., Ltd. (Grant No. IO201229-08274-01), and the Austrian Science Fund (FWF) under Grant No. I04917. The Institute of Engineering Research at Seoul National University provided additional research facilities for this work.

[1] T. Shinjo, T. Okuno, R. Hassdorf, K. Shigeto, and T. Ono, Science **289**, 5481 (2000).
[2] R. P. Cowburn, D. K. Koltsov, A. O. Adeyeye, M. E. Welland, and D. M. Tricker, Phys. Rev. Lett. **83**, 1042 (1999).
[3] T. H. R. Skyrme, Nucl. Phys. **31**, 556 (1962).
[4] A. A. Belavin and A. M. Polyakov, JETP Lett. **22**, 245 (1975).
[5] U. K. Rößler, A. N. Bogdanov, and C. Pfleiderer, Nature (London) **442**, 797 (2006).
[6] A. Bogdanov and A. Hubert, J. Magn. Magn. Mater. **195**, 182 (1999).
[7] M. Finazzi, M. Savoini, A. R. Khorsand, A. Tsukamoto, A. Itoh, L. Duò, A. Kirilyuk, Th. Rasing, and M. Ezawa, Phys. Rev. Lett. **110**, 177205 (2013).
[8] S. Komineas and N. Papanicolaou, Phys. Rev. B **92**, 064412 (2015).
[9] G. Finocchio, F. Buttner, R. Tomasello, M. Carpentieri, and M. Klaui, J. Phys. D: Appl. Phys. **49**, 423001 (2016).
[10] X. Zhang, Y. Zhou, K. M. Song, T.-E. Park, J. Xia, M. Ezawa, X. Liu, W. Zhao, G. Zhao, and S. Woo, J. Phys.: Condens. Matter **32**, 143001 (2020).
[11] C. Back, V. Cros, H. Ebert, K. Everschor-Sitte, A. Fert, M. Garst, T. Ma, S. Mankovsky, T. L. Monchesky, M. Mostovoy, N. Nagaosa, S. S. P. Parkin, C. Pfleiderer, N. Reyren, A. Rosch, Y. Taguchi, Y. Tokura, K. von Bergmann, and J. Zang, J. Phys. D: Appl. Phys. **53**, 363001 (2020).
[12] X. Z. Yu, N. Kanazawa, W. Z. Zhang, T. Nagai, T. Hara, K. Kimoto, Y. Matsui, Y. Onose, and Y. Tokura, Nat. Commun. **3**, 988 (2012).
[13] S. Woo, K. Litzius, B. Krüger, M.-Y. Im, L. Caretta, K. Richter, M. Mann, A. Krone, R. M. Reeve, M. Weigand, P. Agrawal, I. Lemesh, M.-A. Mawass, P. Fischer, M. Kläui, and G. S. D. Beach, Nat. Mater. **15**, 501 (2016).
[14] J. Kim, J. Yang, Y.-J. Cho, B. Kim, and S.-K. Kim, Sci. Rep. **7**, 45185 (2017).
[15] J. Sampaio, V. Cros, S. Rohart, A. Thiaville, and A. Fert, Nat. Nanotechnol. **8**, 839 (2013).
[16] J. Iwasaki, M. Mochizuki, and N. Nagaosa, Nat. Commun. **4**, 1463 (2013).
[17] M. Mochizuki, Phys. Rev. Lett. **108**, 017601 (2012).
[18] Y. Onose, Y. Okamura, S. Seki, S. Ishiwata, and Y. Tokura, Phys. Rev. Lett. **109**, 037603 (2012).
[19] M. Mruczkiewicz, M. Krawczyk, and K. Y. Guslienko, Phys. Rev. B **95**, 094414 (2017).
[20] M. Mruczkiewicz, P. Gruszecki, M. Krawczyk, and K. Y. Guslienko, Phys. Rev. B **97**, 064418 (2018).
[21] J.-V. Kim, F. Garcia-Sanchez, J. Sampaio, C. Moreau-Luchaire, V. Cros, and A. Fert, Phys. Rev. B **90**, 064410 (2014).
[22] M. Beg, R. Carey, W. Wang, D. Cortés-Ortuño, M. Vousden, M.-A. Bisotti, M. Albert, D. Chernyshenko, O. Hovorka, R. L. Stamps, and H. Fangohr, Sci. Rep. **5**, 17137 (2015).

[23] B. Zhang, W. Wang, M. Beg, H. Fangohr, and W. Kuch, Appl. Phys. Lett. **106**, 102401 (2015).

[24] H. Vigo-Cotrina and A. P. Guimarãesa, J. Magn. Magn. Mater. **507**, 166848 (2020).

[25] D. Bhattacharya, M. Al-Rashid, and J. Atulasimha, Sci. Rep. **6**, 31272 (2016).

[26] Y. Nakatani, M. Hayashi, S. Kanai, S. Fukami, and H. Ohno, Appl. Phys. Lett. **108**, 152403 (2016).

[27] Y. Liu, H. Du, M. Jia, and A. Du, Phys. Rev. B **91**, 094425 (2015).

[28] N. Romming, C. Hanneken, M. Menzel, J. E. Bickel, B. Wolter, K. von Bergmann, A. Kubetzka, and R. Wiesendanger, Science **341**, 636 (2013).

[29] I. Dzyaloshinskii, J. Phys. Chem. Solids **4**, 241 (1958).

[30] T. Moriya, Phys. Rev. **120**, 91 (1960).

[31] S. Mühlbauer, B. Binz, F. Jonietz, C. Pfleiderer, A. Rosch, A. Neubauer, R. Georgii, and P. Boni, Science **323**, 915 (2009).

[32] X. Z. Yu, N. Kanazawa, Y. Onose, K. Kimoto, W. Z. Zhang, S. Ishiwata, Y. Matsui, and Y. Tokura, Nat. Mater. **10**, 106 (2011).

[33] I. Kézsmárki, S. Bordács, P. Milde, E. Neuber, L. M. Eng, J. S. White, H. M. Rønnow, C. D. Dewhurst, M. Mochizuki, K. Yanai, H. Nakamura, D. Ehlers, V. Tsurkan, and A. Loidl, Nat. Mater. **14**, 1116 (2015).

[34] M. Hoffmann, B. Zimmermann, G. P. Müller, D. Schürhoff, N. S. Kiselev, C. Melcher, and S. Blügel, Nat. Commun. **8**, 308 (2017).

[35] W. Jiang, P. Upadhyaya, W. Zhang, G. Yu, M. B. Jungfleisch, F. Y. Fradin, J. E. Pearson, Y. Tserkovnyak, K. L. Wang, O. Heinonen, S. G. E. te Velthuis, and A. Hoffmann, Science **349**, 283 (2015).

[36] O. Boulle, J. Vogel, H. Yang, S. Pizzini, D. de Souza Chaves, A. Locatelli, T. O. Menteş, A. Sala, L. D. Buda-Prejbeanu, O. Klein, M. Belmeguenai, Y. Roussigné, A. Stashkevich, S. M. Chérif, L. Aballe, M. Foerster, M. Chshiev, S. Auffret, I. M. Iron, and G. Gaudin, Nat. Nanotechnol. **11**, 449 (2016).

[37] O. V. Pylypovskyi, D. Makarov, V. P. Kravchuk, Y. Gaididei, A. Saxena, and D. D. Sheka, Phys. Rev. Appl. **10**, 064057 (2018).

[38] V. P. Kravchuk, D. D. Sheka, A. Kákay, O. M. Volkov, U. K. Rößler, J. van den Brink, D. Makarov, and Y. Gaididei, Phys. Rev. Lett. **120**, 067201 (2018).

[39] V. P. Kravchuk, U. K. Rössler, O. M. Volkov, D. D. Sheka, J. van den Brink, D. Makarov, H. Fuchs, H. Fangohr, and Y. Gaididei, Phys. Rev. B **94**, 144402 (2016).

[40] Y. Gaididei, V. P. Kravchuk, and D. D. Sheka, Phys. Rev. Lett. **112**, 257203 (2014).

[41] V. L. Carvalho-Santos, R. M. Corona, D. Altbir, and S. Castillo-Sepúlveda, Phys. Rev. B. **102**, 024444 (2020).

[42] J. Yang, C. Abert, D. Suess, and S.-K. Kim, Sci. Rep. **11**, 3886 (2021).

[43] S. S. P. Parkin, K. P. Roche, M. G. Samant, P. M. Rice, and R. B. Beyers, J. Appl. Phys. **85**, 5828 (1999).

[44] M. He, G. Li, Z. Zhu, Y. Zhang, L. Peng, R. Li, J. Li, H. Wei, T. Zhao, X.-G. Zhang, S. Wang, S.-Z. Lin, L. Gu, G. Yu, J. W. Cai, and B.-G. Shen, Phys. Rev. B **97**, 174419 (2018).

[45] A. S. Szalay, J. Gray, G. Fekete, P. Z. Kunszt, P. Kukol, and A. Thakar, arXiv:cs/0701164.

[46] With $h = R$, we found that the core of skyrmions would be slightly displaced from the shell's geometric center due to nonuniform finite-element meshes.

[47] C. Abert, L. Exl, F. Bruckner, A. Drews, and D. Suess, J. Magn. Magn. Mater. **345**, 29 (2013).

[48] L. D. Landau and E. M. Lifshitz, Phys. Z. Sowjetunion **8**, 153 (1935); T. L. Gilbert, Phys. Rev. **100**, 1243 (1955).

[49] See Supplemental Material at http://link.aps.org/supplemental/10.1103/PhysRevB.104.134427 for the dynamic modes of the skyrmions in the hemispherical shells: Supplemental Movies 1 and 2 (animations of characteristic eigenmodes of a skyrmion and a skyrmionium); Supplemental Movie 3 (animation of the topological transition from skyrmion to skyrmionium, and vice versa); (S1) transformation of unrolled planar view; (S2) phase diagram of the variation of spin textures for different shell diameters; (S3) curved geometry effect on the stability of skyrmion; (S4) dynamic motions of skyrmion and skyrmionium driven by resonant AC fields.

[50] N. Papanicolaou and T. N. Tomaras, Nucl. Phys. **360**, 425 (1991).

[51] F. Garcia-Sanchez, P. Borys, A. Vansteenkiste, J.-V. Kim, and R. L. Stamps, Phys. Rev. B **89**, 224408 (2014).

[52] G. Siracusano, R. Tomasello, A. Giordano, V. Puliafito, B. Azzerboni, O. Ozatay, M. Carpentieri, and G. Finocchio, Phys. Rev. Lett. **117**, 087204 (2016).

[53] X. Zhang, J. Xia, Y. Zhou, D. Wang, X. Liu, W. Zhao, and M. Ezawa, Phys. Rev. B **94**, 094420 (2016).

[54] F. Zheng, H. Li, S. Wang, D. Song, C. Jin, W. Wei, A. Kovács, J. Zang, M. Tian, Y. Zhang, H. Du, and R. E. Dunin-Borkowski, Phys. Rev. Lett. **119**, 197205 (2017).

[55] S. Rohart and A. Thiaville, Phys. Rev. B **88**, 184422 (2013).

[56] A. De Lucia, K. Litzius, B. Krüger, O. A. Tretiakov, and M. Kläui, Phys. Rev. B **96**, 020405(R) (2017).

[57] The errors of threshold *D*th values are limited by the mesh size of the simulations, so here the minimum surface node distance of 1 nm was maintained for all the simulations.

[58] J. Yang, J. Kim, C. Abert, D. Suess, and S.-K. Kim, Phys. Rev. B **102**, 094439 (2020).

[59] P. J. Metaxas, J. P. Jamet, A. Mougin, M. Cormier, J. Ferre, V. Baltz, B. Rodmacq, B. Dieny, and R. L. Stamps, Phys. Rev. Lett. **99**, 217208 (2007).

[60] H.-B. Jeong and S.-K. Kim, Appl. Phys. Lett. **105**, 222410 (2014).

[61] K. Y. Guslienko, A. N. Slavin, V. Tiberkevich, and S.-K. Kim, Phys. Rev. Lett. **101**, 247203 (2008).

[62] H.-K. Park, J.-H. Lee, J. Yang, and S.-K. Kim, J. Appl. Phys. **127**, 183906 (2020).

[63] K.-S. Lee, S. Choi, and S.-K. Kim, Appl. Phys. Lett. **87**, 192502 (2005).

[64] K.-S. Lee and S.-K. Kim, Phys. Rev. B **78**, 014405 (2008).

[65] S. Komineas and N. Papanicolaou, Phys. Rev. B **92**, 174405 (2015).

[66] C. Song, Y. Ma, C. Jin, J. Wang, H. Xia, J. Wang, and Q. Liu, New J. Phys. **21**, 083006 (2019).

[67] O. V. Pylypovskyi, D. D. Sheka, V. P. Kravchuk, F. G. Mertens, and Y. Gaididei, Phys. Rev. B **88**, 014432 (2013).

[68] P. Fischer, D. Sanz-Hernández, R. Streubel, and A. Fernández-Pacheco, APL Mater. **8**, 010701 (2020).

[69] A. Fernández-Pacheco, R. Streubel, O. Fruchart, R. Hertel, P. Fischer, and R. P. Cowburn, Nat. Commun. **8**, 15756 (2017).

[70] A. Albrecht, G. Hu, I. L. Guhr, T. C. Ulbrich, J. Boneberg, P. Leiderer, and G. Schatz, Nat. Mater. **4**, 203 (2005).

[71] T. C. Ulbrich, D. Makarov, G. Hu, I. L. Guhr, D. Suess, T. Schrefl, and M. Albrecht, Phys. Rev. Lett. **96**, 077202 (2006).
[72] F. Tejo, D. Toneto, S. Oyarzún, J. Hermosilla, C. S. Danna, J. L. Palma, R. B. da Silva, L. S. Dorneles, and J. C. Denardin, ACS Appl. Mater. Interfaces **12**, 53454 (2020).
[73] P. F. Carcia, J. Appl. Phys. **63**, 5066 (1988).
[74] S.-K. Kim and J. B. Kortright, Phys. Rev. Lett. **86**, 1347 (2001).
[75] R. Krishnan and H. Lassri, J. Appl. Phys. **73**, 6433 (1993).
[76] A. Simopoulos, E. Devlin, A. Kostikas, A. Jankowski, M. Croft, and T. Tsakalakos, Phys. Rev. B **54**, 9931 (1996).